Polymer 69 (2015) 148–158

Contents lists available at ScienceDirect

Polymer

journal homepage: www.elsevier.com/locate/polymer

Structural hierarchy and surface morphology of highly drawn ultra high molecular weight polyethylene fibers studied by atomic force microscopy and wide angle X-ray diffraction

Preston B. McDaniel [a, b], Joseph M. Deitzel [a, *], John W. Gillespie Jr. [a, b, c, d]

[a] Center for Composite Materials, University of Delaware, DE, USA
[b] Department of Materials Science and Engineering, University of Delaware, DE, USA
[c] Department of Mechanical Engineering, University of Delaware, DE, USA
[d] Department of Civil and Environmental Engineering, University of Delaware, DE, USA

ARTICLE INFO

Article history:
Received 16 February 2015
Received in revised form
27 April 2015
Accepted 7 May 2015
Available online 18 May 2015

Keywords:
Ultra high molecular weight polyethylene
High performance fibers
Nanostructure

ABSTRACT

The meso/nanostructure of UHMWPE fibers manufactured using different processing conditions is explored through atomic force microscopy (AFM) and wide-angle X-ray diffraction (WAXD). Characteristic dimensions of sub-filament microstructure are quantified at the fiber surface and the fiber interior. These measurements are compared to crystalline parameters determined using WAXD. Observation of junctions between microfibrils suggests the original gel network from which the fiber was drawn remain in the final product. For fibers having undergone greater drawing, the fiber surface reveals the presence of large-scale epitaxial features oriented perpendicular to the direction of drawing. Annealing experiments show that epitaxial structures undergo thickening at temperatures >120 °C. Examining fiber cross-sections reveals a network of microfibrils that appear to undergo consolidation with increased drawing. The evolution of the structural hierarchy of these fibers is discussed in the context of its implications for optimization of processing both fibers and their composites.

1. Introduction

Ultra high molecular weight polyethylene fibers are commonly used in composite materials due to their high specific strength and stiffness in tension [1–3]. These high performance fibers derive their strength and stiffness from aligned molecular chains. With very large molecular weights, the high aspect ratio polymer is able to crystallize in extended chain morphologies under appropriate processing conditions [4–9]. The UHMWPE is able to transfer stress along the C–C backbone, but lateral interactions between molecules is only through van der Waals forces [10–13]. The result is a highly anisotropic material with stiffness and strength orders of magnitude lower transverse to the molecular axis when compared to axial tensile properties. Incorporation of these fibers into composite materials aids in transferring off-axis loads while still taking advantage of the mechanical properties along the fiber axis. The strength and stiffness of these materials is highly dependent on phase morphology and in turn the processing conditions to bring about such structural features. While macroscopic mechanical behavior of UHMWPE fibers is of utmost importance in the discussion of composites applications, the basis of their performance is derived from the meso/nanostructural components.

As illustrated in Fig. 1, previous research has described a multiscale fibrillar hierarchy composing a single UHMWPE fiber grown or manufactured by various procedures [1,14,15]. At the smallest scale there are fibrillar crystals present in solution grown and gel spun fibers. Based on spectroscopic, X-ray and electron diffraction, and solid-state NMR results it has been shown that the fibrillar crystals are composed of both crystalline and non-crystalline material in series along the fiber axis [16–18]. In the fiber these are often thought to be the main component of microfibrils which are actually only 10's of nanometers in diameter on average. The microfibrils are then grouped into larger macrofibrils on the order of 100's of nm to several micrometers [1,14]. In the early stages of draw, gel spun fibers often exhibit shish-kebab morphologies where the shish-kebab is composed of a more thermodynamically stable extended-chain “shish” and the lamellar “kebab” crystal epitaxially crystallizes on the surface [19–21]. However, during the

* Corresponding author.
E-mail address: jdeitzel@udel.edu (J.M. Deitzel).

http://dx.doi.org/10.1016/j.polymer.2015.05.010
0032-3861/

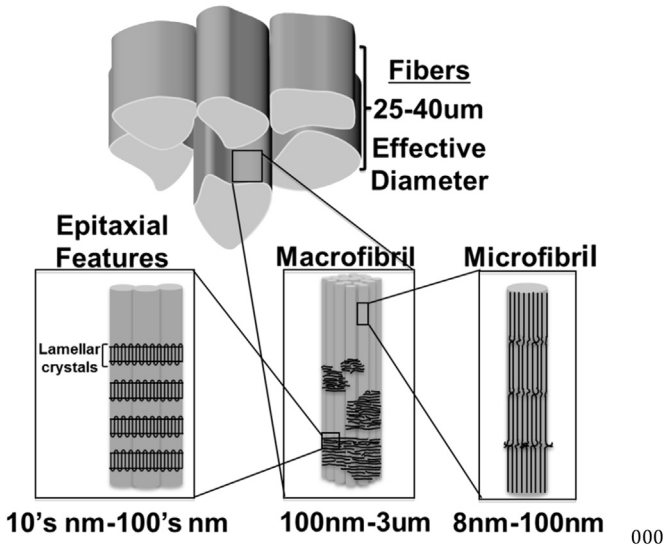

Fig. 1. Structural hierarchy of UHMWPE fibers with multiple levels of fibrillar structure.

drawing process the lamellar crystals of the shish-kebab are drawn and incorporated into the extended chain regime of the fibrillar crystal [22]. The type of high draw ratios and elevated temperature at which this occurs is key to the development of the extended chain morphologies from which the fiber derives high strength and stiffness. Other research has revealed the presence of these epitaxial structures on the surface of highly drawn fibers [23,24], raising the question of their origin and significance in the discussion of structure/property relationships. As these fibers are incorporated into composite materials, a key metric in determining their effectiveness in load bearing and impact resistance is their ability to absorb and dissipate energy.

Energy absorption and dissipation begins at the nanoscale with load pathways originating in the fibrillar structure. In tension, load is transferred both along the axis of fibrils and likely through shear between adjacent fibrillar crystals as well [25–27]. In the discussion of fiber mechanical behavior, it is important to also look beyond the nanoscale fibrils to mesoscale characteristics. While the load pathways through crystalline and intercrystalline material have been studied, there is still much to learn about the spatial distribution and interconnectivity of the microfibrils and the manner in which their interactions control energy dissipation. Voids, misalignments and fibrillar junctions at this scale may significantly influence both the stiffness and strength of the fiber. Beyond the structure/property relationships found within the fiber, the interaction of fiber and matrix in a composite material provide another mechanism for energy dissipation. Previous research has demonstrated the importance of fiber topography in this situation [28]. Under impact, fibers are typically pulled into the impact zone, leading to shear deformation between the fiber and resin [29]. The result is that fiber surface morphology directly influences the interfacial strength during fiber pullout.

The important first step in understanding structure/property relationships of a material is to identify the fundamental structural units. In the case of UHMWPE fibers, the geometry and spatial distribution of the meso/nanoscale morphological features are key to the macroscale mechanical properties of interest, but still not completely understood. The nanoscale fibrillar crystals which compose the fiber are often considered the fundamental building block of these fibers, but knowledge of their characteristic size and interconnectivity in high tenacity fibers is lacking. In addition, the appearance of epitaxial structures on the surface of highly drawn fibers has been noted [23,24] and a deeper understanding of their origin may provide valuable insight into the evolution of the interior structure of a fiber under common processing conditions. Through the comparison of high resolution microscopy techniques and wide angle X-ray diffraction, the research herein aims to quantify dimensions of fibrillar crystals and epitaxial features as well as provide some insight into the nano and mesoscale interactions between fibrils. Three fibers of different processing histories, and consequently different mechanical properties, are studied in order to understand the structural differences that influence the change in macroscopic mechanical properties. Ultimately, fundamental changes in meso/nanoscale morphologies are discussed in the context of energy dissipative capabilities.

2. Experimental

Three fibers provided by Honeywell International Inc. are used in this study. The linear density and tenacity of the fibers in their as-given tow are reported in Table 1. Linear density is mass per unit length. Typically, linear density is reported in units of "denier", which is the mass in grams per 9000 m. A reduction in linear density of a fiber directly correlates to an increase in the amount of drawing the filament has undergone. So the relative changes in linear densities observed in Table 1 , reflect the relative differences in the amount of drawing between each filament type. Tenacity, a measure of strength, is the breaking force normalized by the linear density, each of which are defined according to ASTM standard D3822 [30] and D1577 [31] respectively. Mechanical property data was obtained for single fibers using an Instron Micro Tester 5848 and a 5 N load cell using a set of pneumatic cord grips and a 4-inch gauge length.

The 12.23 denier sample, from this point forward will be referred to as the Precursor fiber, while the 5.18 Denier sample will be referred to as the Post Draw fiber. These fibers come from the same batch of material, but have been removed at different points along the drawing line. The highest tenacity and lowest linear density fiber, S130, is a commercial grade fiber that is included for comparison. These fibers are produced through a multistage drawing process with the highest draw ratios occurring at elevated temperatures [32]. It is important to note that each of these fiber types is highly drawn. The main difference between the Precursor and Post Draw, and Commercial S130 fibers is that the latter materials have undergone an additional drawing at elevated temperatures [32].

Samples are prepared for microscopy study by mounting single polyethylene fibers to an aluminum puck with carbon tape. Fibers are removed from a tow by careful teasing using a pair of tweezers. Special care is given not to bend the fibers so as to introduce kink bands or touch the portion of the fiber surface used in imaging. Macroscopic fiber imaging was performed with a Keyence VK-X200 3D Laser Scanning Confocal Microscope and a Skyscan 1172 Micro-CT with 0.6 μm/pixel resolution at a 40 kV operating voltage.

A Bruker Dimension Icon atomic force microscope with a Nanoscope V controller was used in this study. Imaging was performed using the Peak Force Tapping method in PF QNM. This is a contact type imaging method where minimal force is applied to the tip by creating a force/displacement measurement at each point of contact [33]. Using this imaging method along with a low spring constant cantilever, minimal surface disruption may be achieved. To this end, a probe with a 2 nm nominal radius has been used in these experiments. In this way minimal surface disruption is achieved with resolution on the order of tip diameter.

Measurement of feature dimensions is made through the use of Nanoscope Analysis software provided by Bruker. The cross-section

Table 1
Physical properties of 3 fibers tested.

Fiber	Effective diameter (μm)	Fiber linear density (denier)	Maximum load (gf)/(N)	Tenacity/Strength (gf/den)/(GPa)[a]
Precursor	42.23 ± 0.15	12.23 ± 1.00	366.80 ± 33.02/ 3.60 ± 0.32	29.99 ± 3.65/ 2.56 ± 0.23
Post-Draw	27.51 ± 0.07	5.19 ± 0.31	221.53 ± 26.98/ 2.17 ± 0.26	42.68 ± 5.79/ 3.65 ± 0.44
S130	21.26 ± 0.08	3.10 ± 0.29	139.32 ± 13.46/ 1.37 ± 0.13	44.84 ± 6.04/ 3.86 ± 0.37

[a] Units of GPa give a measure of strength. This average strength is approximate because of the irregular cross-section and is estimated using an effective diameter.

tool allows observation of the topography data so that measurements may be made directly from the raw data. The curved and irregular nature of the fiber surface can make it difficult to examine small features due to the extreme height changes. To account for natural curvature on the fiber surface, images are adjusted with a 3rd order plane fit using the Nanoscope Analysis software. This adjustment to the raw data alters the height of the features, but leaves the dimensions in the x–y plane unaltered. All measurements of microfibril widths and annealed epitaxial features are performed with a 3.8 nm pixel resolution. This readily allows measurement of structural features at the surface. However, in the case of some small features, it is possible that error on the order of tip radius is possible. In the case of microtomed fibers, a flat surface is achieved and only a 1st order plane fit is used to remove sample tilt. Finally, after all measurements have been made, a wavelet deconvolution filter is applied to the AFM images using Astra Image 4.0 software [34]. This step is performed to clarify features of interest for the purpose of discussion.

Annealing experiments were performed on a heating stage mounted within the acoustic hood of the AFM. The stage was calibrated and found to be accurate within 0.5 °C. Samples were heated to final temperature in approximately 3 min. Then samples were held at temperature for 15 min in order for the temperature to equilibrate throughout the entire sample. Finally, samples are cooled under ambient conditions.

Samples were embedded in a low viscosity Spurr resin under vacuum to promote complete encapsulation and avoid microbubbles. The resin is then cured at 70 °C, well below the onset of melting in the fibers. Fibers were microtomed using a Leica Ultracut UCT and a Delaware Diamond Knives ultramicrotome diamond blade. Fibers are microtomed along the axis and perpendicular to the axis in order to obtain an idea of the three dimensional structure of the meso/nanostructure. The fibers are microtomed until the center of the fiber is reached, and then the microtomed surface is imaged by AFM.

Wide-angle X-ray diffraction experiments were performed with a Bruker D8 Discover system and a Vantec 2D detector along with a copper radiation source and 0.5 mm graphite collimator. Samples were collected in transmission at a 200 mm distance. Two types of samples were prepared for each fiber type examined. First, a bundle of fibers were mounted vertically in a manner that fiber overlap was minimized. Then, single fibers were mounted vertically so that crystalline orientation might be measured. Diffraction patterns were integrated using Bruker EVA analysis software along 2 theta and gamma (Fig. 2).

3. Results and discussion

3.1. Wide angle X-ray diffraction

The crystalline structure and geometry was first studied by WAXD. The 2D and 1D diffraction pattern are shown in Fig. 2. The peaks are indexed according to their corresponding scattering planes for orthorhombic and monoclinic crystals in the fiber [35,36]. While there is some amount of monoclinic crystal phase present in each fiber type, it is calculated to be less than 4 percent of the total area under the diffraction curve, with the majority of crystalline material within the fiber being orthorhombic [37]. To calculate effective scattering domain sizes, the Scherrer Equation was used [38]. Dimensions in the [200], [020], and [110] directions were calculated and compared in Table 2.

The domain sizes in [200], [020], and [110] all increase with increasing draw. The lateral thickening of domains with increasing draw is consistent with results in the literature [37,39]. Each of these dimensions are perpendicular to the fiber axis, corresponding to microfibril widths in real space. Each measurement, with the exception of the S130 crystallite size in [110], falls in the 20–40 nm range. These dimensions will serve as baseline values for comparison with further AFM measurements. In doing so, it is important to remember that WAXD yields volume average dimensions of effective scattering domain size, whereas direct measurements may be made with AFM.

Along with scattering domain dimensions, the percent crystallinity and relative crystal alignment were all calculated from WAXD results. The percent crystallinity was not significantly altered between the three samples, remaining around 85% for each, suggesting that despite changes during processing, the overall crystallinity does not drastically change.

Crystallographic orientation is quantified through calculation of the Herman's Orientation Factor [40]. The orientation of crystals relative to the filament axis is considered to be a key factor in determining tensile properties [41]. The orientation factor, determined from the 2D diffraction pattern of single fibers gives a measure of crystal orientation. In the direction perpendicular to the fiber axis, perfect orientation results in $f = -0.5$ while $f = 1$ corresponds to perfect orientation along the axis [40]. The sum of orientations in the three orthogonal axes of the fiber is zero, allowing calculation of axial orientation after (200) and (020) are found. The results shown in Table 3 indicate very little change in axial orientation as a function drawing with only a slightly higher orientation in the Post-Draw and S130 fibers.

3.2. Surface morphology of highly drawn S130

Initial microscopy studies focused on the morphological features of the high tenacity S130 fiber. It may be reasonably stated that because of the low linear density per fiber and high tenacity, this fiber has undergone the highest degree of draw of the three fibers. Despite a highly drawn and aligned molecular structure, the complexity of the sub-filament structure is first evident at the macroscale. As seen in Fig. 3, single fibers have a surface composed of high and low points across the circumference. The images from the confocal microscope and micro-CT reveal an irregular cross-section, making it difficult to assign a fiber diameter. To overcome this issue, an effective diameter base on linear density may be defined [42]. However, it is important to emphasize that the effective diameter is not exact, and may slightly change with variations in linear density along the length of a fiber.

Further analysis of the surface of the UHMWPE fiber was carried out using AFM in Peak Force QNM mode. Fig. 4 shows an example of a typical AFM scan of the surface of an S130 fiber. Inspection of the image at this scale reveals that the complexity extends to the meso/nanoscale. Microfibrils from 10 to 100 nm are clearly resolved. These fibrils appear to be clustered together into bundles 100's of nm up to several micrometers in width, which give the fiber its corrugated appearance on the surface. A study of similar images revealed considerable variation in macrofibrils above 100 nm in

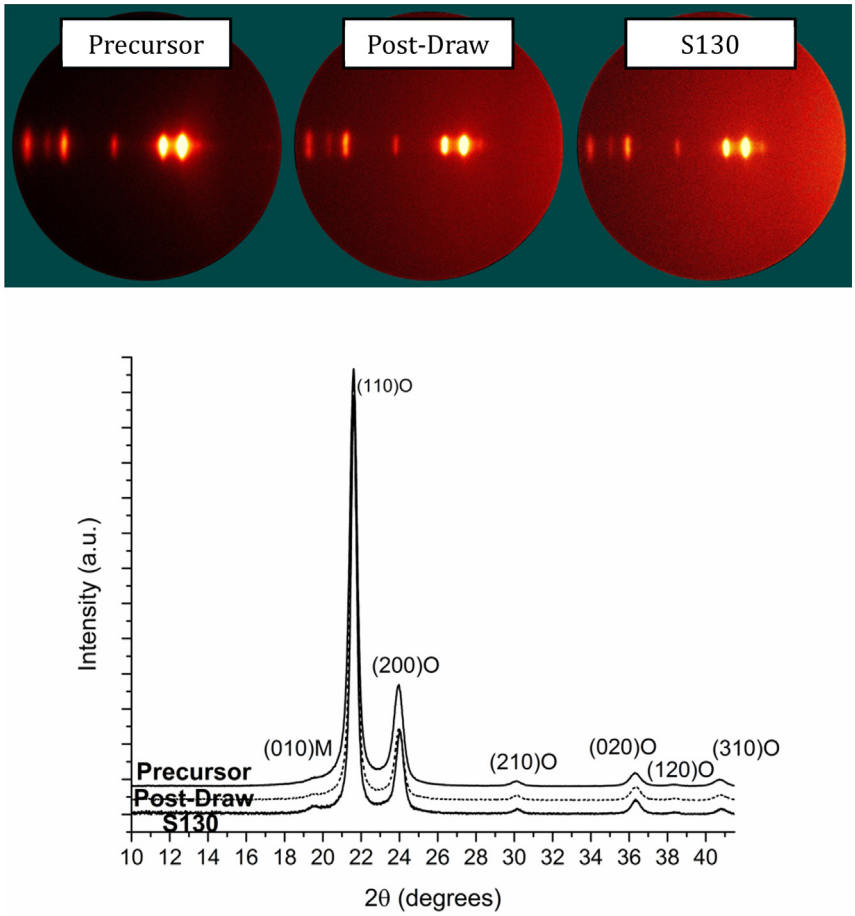

Fig. 2. 2D diffraction patterns of fiber bundles. Integrated WAXD pattern for each of the fiber types examined. Peaks are labeled O for orthorhombic and M for monoclinic. For visualization, intensities are normalized by the (110) peak.

Table 2
Calculated crystal effective crystal domain sizealong with crystallinity and relative crystalline orientation along the fiber axis.

Fiber	(200) dimensions	(020) dimensions	(110) dimensions	Percent crystallinity
Precursor	21.85 nm	18.31 nm	27.35 nm	83%
Post-Draw	22.84 nm	19.84 nm	31.27 nm	87%
S130	30.34 nm	22.80 nm	41.32 nm	85%

Table 3
Herman's orientation factor calculated from WAXD intensities.

Herman's orientation factor (f)			
Crystal plane	Precursor	Post-Draw	S130
200	−0.494	−0.499	−0.499
020	−0.496	−0.499	−0.499
Axial factor	0.991	0.999	0.999

width. However, analysis of the microfibrils on the fiber surface revealed a trend in directly measured widths. When plotted in Fig. 5, the log normal distribution of fibril widths becomes evident. While some microfibrils are measured as small as 16 nm and greater than 90 nm, over 70 percent of the fibrils measured are between 20 and 40 nm. These dimensions, consistent with similar measurements via SEM in the literature [43], correlate quite well with the crystallite dimensions calculated from WAXD measurements. This suggests that the majority of microfibrils are arrays of single crystals linked in series.

3.3. Epitaxial features on S130

In addition to the fibrils on the surface of the fiber, there is clear evidence of what appear to be ordered structures oriented perpendicular to the fiber axis and spanning multiple microfibril widths. These ordered structures appear to be epitaxial crystals on the surface of the underlying fibrillar hierarchy. The epitaxial features are abundant on the surface of the S130 fibers in domain sizes from 100's of nanometers to several micrometers in size, often bridging the gaps between fibrils. AFM measurements, plotted in Fig. 6 give an idea of the distribution of thickness, along the fiber axis, measured for epitaxial structures. The overwhelming majority of features are between 30 and 40 nm thick in the direction of the fiber axis, yielding an average of 35 ± 6 nm. While similar to traditional shish-kebab features in drawn gels of UHMWPE and melt processed fibers, several key differences may be noted. First, shish-kebabs are historically represented as epitaxial folded chain crystals on the surface of a single extended chain crystal. The AFM images of the S130 paint a slightly different picture, with the epitaxial features spanning relatively large distances over multiple microfibrils. Secondly, as previously mentioned, in optimally drawn UHMWPE fibers, shish-kabob, and other epitaxial morphologies are reported to be effectively minimized in occurrence [22]. However, on the surface of these

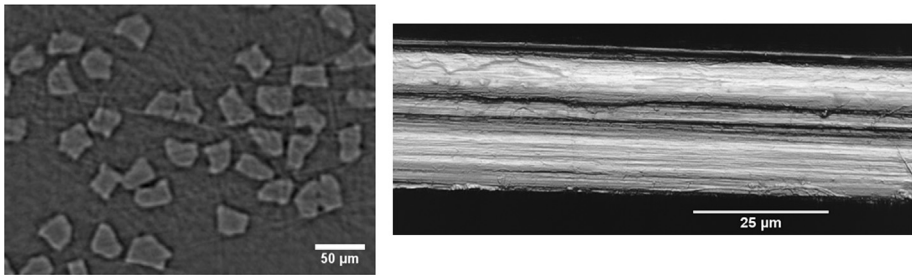

Fig. 3. Micro-CT image shows axial cross-section of multiple fibers in a tow (left). Confocal microscopy image of UHMWPE fiber topography image (right).

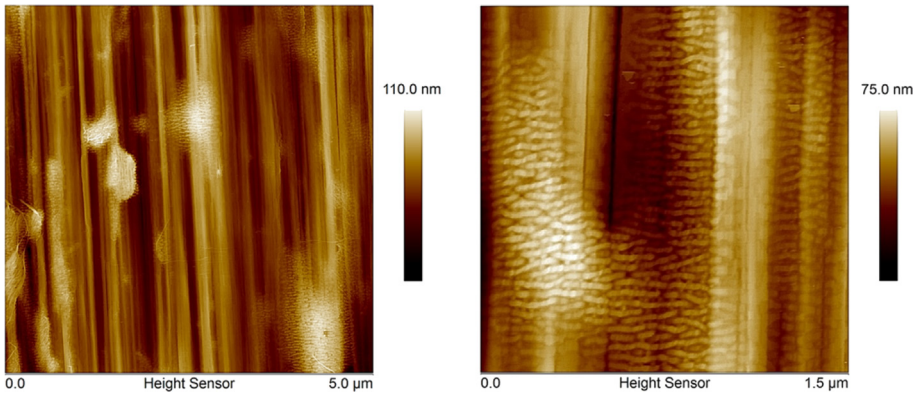

Fig. 4. Fibrillar structure and epitaxial features on the surface of an S130 fiber. 5 um scan on the surface of the fiber (left). 1.5 um scan on a different fiber showing the large domains of epitaxial features (right).

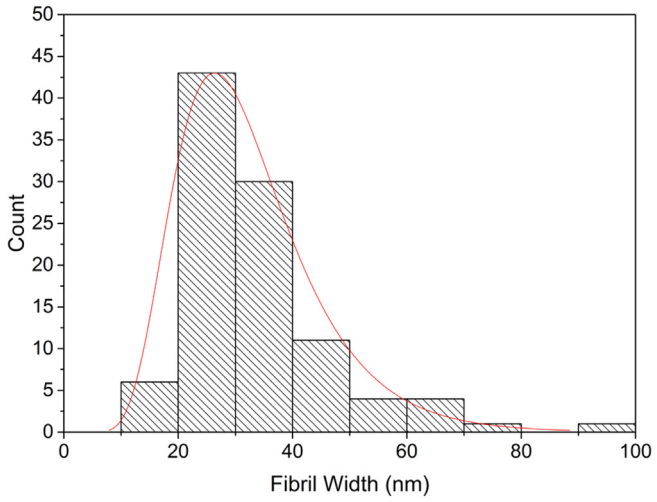

Fig. 5. Microfibril width distribution of high tenacity, 130 denier Spectra fiber. A log normal distribution of fibril widths was measured with the majority of fibrils falling between 20 and 40 nm in width.

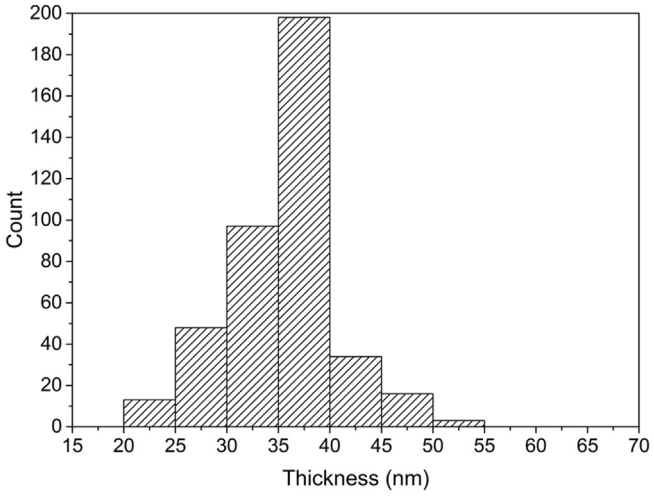

Fig. 6. Distribution of lamellar thickness measured from the surface of multiple fibers.

commercial fibers, they are clearly present and their presence may provide some insight into the evolution of meso/nanostructure in highly drawn fibers.

To further explore the nature of the epitaxial features, a series of annealing experiments was designed. Inspection via AFM was carried out for the same area of the fiber surface before and after the annealing procedure. Annealing was performed in the temperature range common to both drawing temperatures during fiber formation and subsequent composites processing between 115 and 130 °C in 5° increments [32,44]. The changes in epitaxial thickness are presented as a shift in the distribution in Fig. 7. A shift in the distribution of thickness was noticed at each annealing temperature with the greatest changes noticed at 130 °C. Before annealing, a large portion of the epitaxial features are between 35 and 40 nm. After annealing at lower temperatures (115–125 °C) there is a slight shift in the distribution of thickness. The thinner epitaxial features reorganize and are incorporated into thicker features. However, at 130 °C there is a large shift in thickness distribution. All features less than 35 nm have melted, and most importantly, the 35–40 nm crystals which

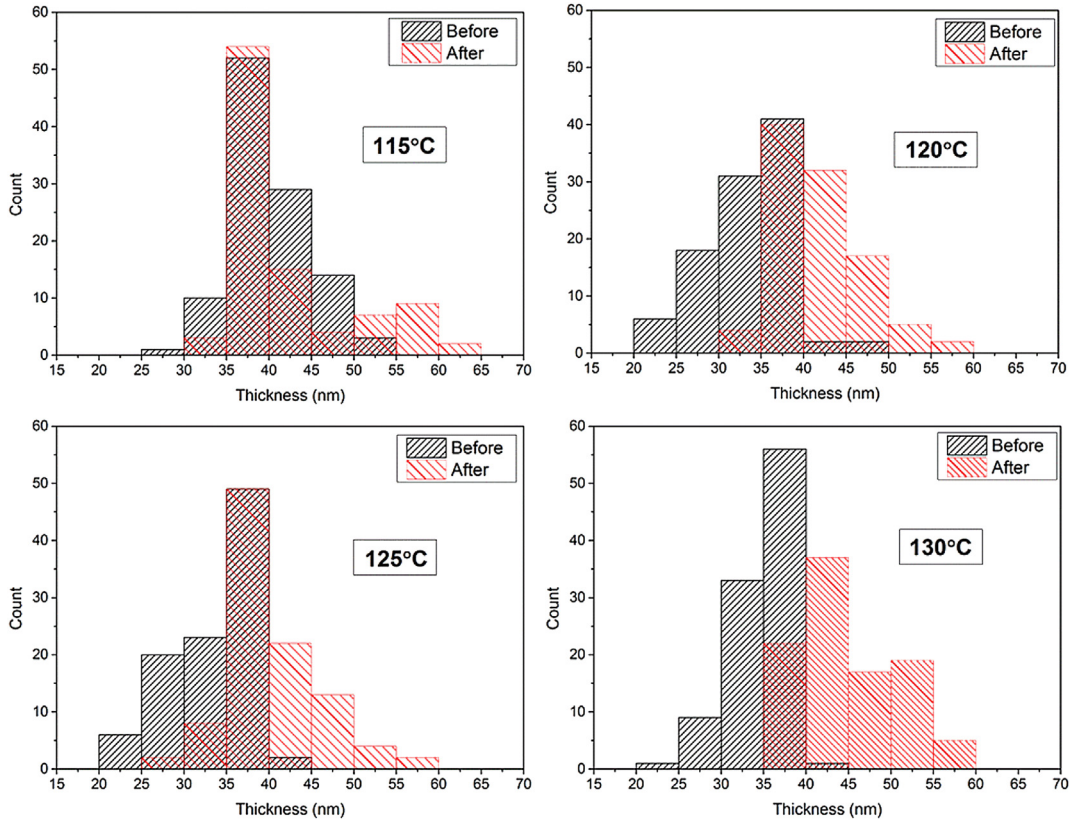

Fig. 7. Changes in epitaxial structure after annealing at common processing temperatures represented as a distribution of thickness measured by AFM.

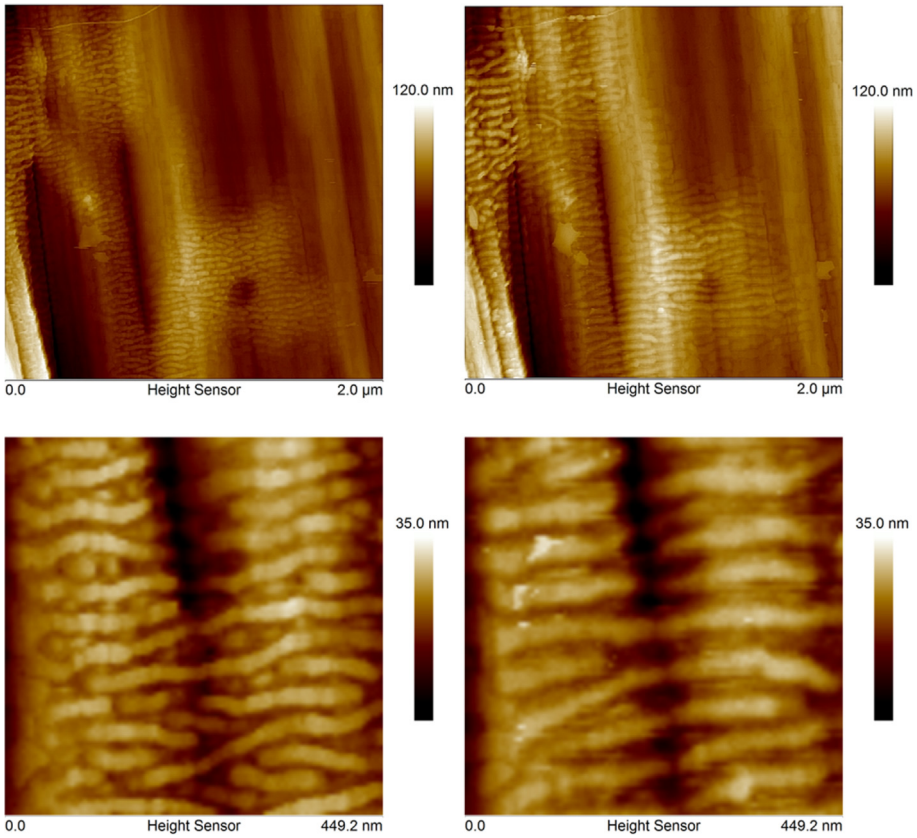

Fig. 8. Reorganization of epitaxial structures after annealing at 130 °C. Images on the left are before annealing and images on the right are after annealing. Images at the bottom are smaller scans of the exact same area on the same fiber.

have remained stable up to this annealing temperature have begun to melt. The significant reorganization at 130 °C is shown in Fig. 8.

Several conclusions may be drawn from this series of annealing experiments. First, the observed reorganization of these structures as a function of temperature is consistent with annealing behavior of chain folded lamellar crystals. From the data it is apparent that the majority of these structures are stable up to a temperature of approximately 130 °C, which is also consistent with the melting of lamellar crystals [45]. One possibility for the origin of these crystals on the surface is excess low molecular weight oligomer used as a processing aid. However, the relative stability of the predominant 35–40 nm crystals for temperatures exceeding 130 °C suggests the lamellar crystals are polymeric in nature, as opposed crystallization of short chain oligomers, which would have a much lower melting temperature.

It is worth noting that the proliferation of epitaxial crystals on a UHMWPE fiber surface has implications for energy dissipation in a composite, as Gao et al. [28] has demonstrated concerning the effects of surface roughness on fiber pullout. Finally, the consolidation of lamellar crystals implies enhanced interconnectivity of fibrils at the surface. If, in fact, the epitaxial crystals are composed of polymeric material as suggested by the annealing experiments, it is likely that they share polymer chains with the underlying microfibrils. Then the epitaxial crystals act as bridges between adjacent microfibrils providing a form of physical interaction of fibrils within a given domain of epitaxial features. The exact nature of the connectivity between the chain folded lamellar and the underlying microfibrils and its effect on fiber mechanical properties will be the subject of future research.

The question regarding the mechanism by which these surface structures are formed remains. There are three likely scenarios one may consider, which may result in the epitaxial UHMWPE crystals. First, under very large extensions it is possible that some polymer chains are extended to the point that a chain end becomes free of the fibrillar crystal, allowing incorporation into a lamellar crystal. Second, very high draw ratios may result in the fracture of microfibrils. These fractured microfibrils would then be free of mechanical constraints that effectively stabilize the microfibril, allowing melting to occur. The lack of physical constraint would enable melting and recrystallization as chain folded lamellar crystals when the fibers are cooled. A third possibility is that these structures originate in part from surface melting of larger, stable microfibrils during the drawing process. From the annealing experiment, we can infer that the S130 fibers see temperatures in excess of 130 °C during drawing. Wunderlich [46] demonstrated that chain folded crystals could be grown on the fracture surface of extended chain crystals by annealing the fracture surface at temperatures (120 °C) approaching the onset of melting. While not specifically discussed in the context of polyethylene fibers, the same conditions may be present at the surface of a microfibril where areas on the uneven fiber surface are exposed. It is likely that each of these mechanisms contribute to the final surface morphology of the drawn fiber.

3.4. Precursor and Post-Draw fibers

In order to further understand fiber morphology and the mechanisms governing the formation of epitaxial features on the surface of highly drawn UHMWPE fibers, two other fibers were

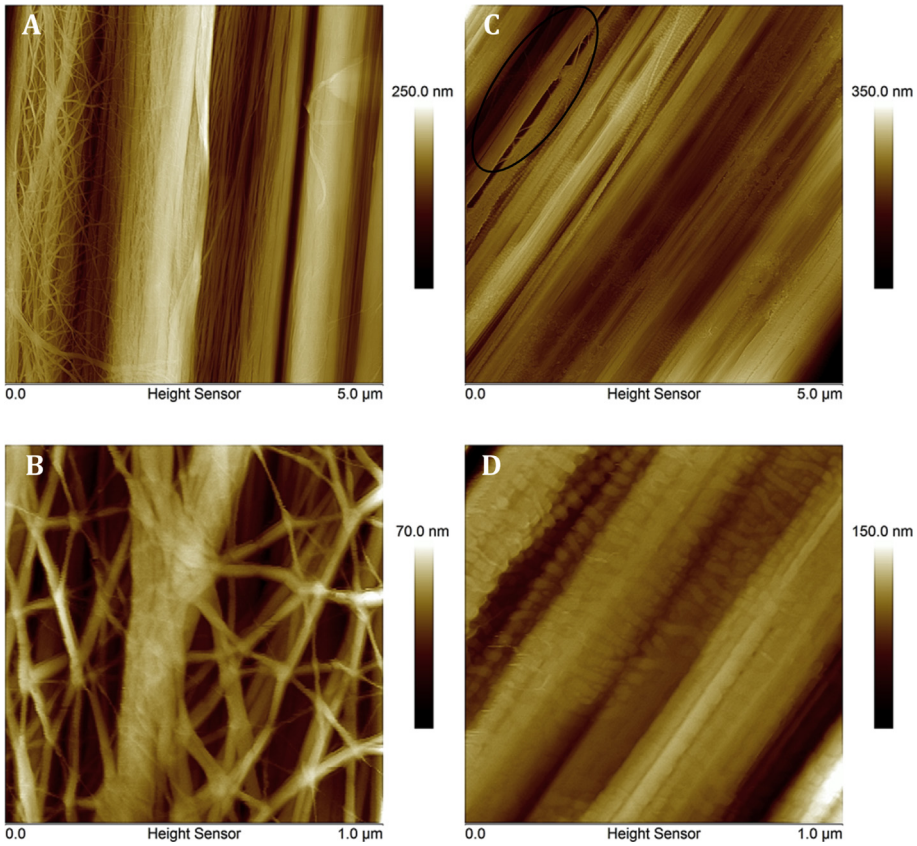

Fig. 9. Precursor and Post-Draw fibers AFM images. A) Precursor fiber surface. B) Smaller scan area from Image A showing evidence of a network structure with multiple fibril junctions. C) Post-Draw fiber surface. D) Smaller scan area from Image C to demonstrate the presence of epitaxial crystals on the fiber surface.

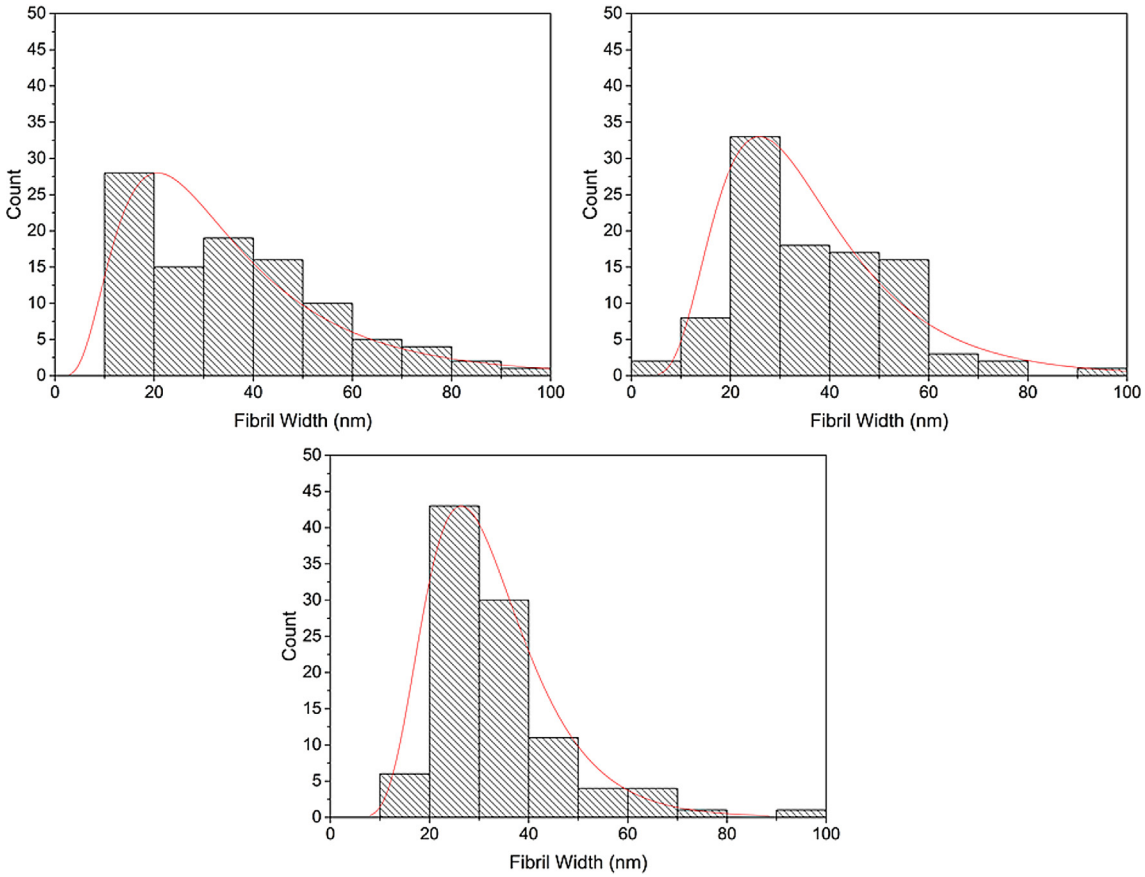

Fig. 10. Microfibril distribution in 12.23 denier Precursor (left), 5.19 denier Post-Draw fiber (right) and 3.10 denier S130 (bottom).

examined. The Precursor and Post-Draw fibers provide insight into the evolution of structural features with increasing draw. As discussed in the Experimental section, these fiber have been taken from different points on the same processing line. Both fibers have undergone drawing, the Post-Draw to a larger extent. Fig. 9 shows AFM images of the surface of each fiber. The AFM images clearly illustrate differences in meso/nanostructure of the two fibers. The first, and most obvious difference between the two, is the relative degree of microfibril alignment. While the Post-Draw fiber exhibits a well-aligned fibrillar structure, the microfibrils of the Precursor fiber surface slightly deviate from the fiber axis. This tracks well with WAXD results that indicate increased crystal alignment in the Post-Draw fiber. However, the alignment of microfibrils extends beyond the nanoscale alignment of crystals. As the length of a polycrystalline microfibril is tracked along the fiber axis, it may be thought of as a mesoscale structure. Misalignments on this length scale (micrometers) have a more profound effect on the mechanical behavior of the macroscopic fiber.

Misalignment on the surface of the Precursor fiber provides a unique opportunity to examine the fibrillar structure. As seen in Fig. 9B, a network structure exists at the microfibril level. Junctions between multiple microfibrils are seen along the imaged area. These junctions often consist of three or more sections of microfibrils meeting and branching off, much like a net. Earlier work on the gel state of polymers has shown that fibers produced through gel-spinning and similar techniques originate from a network structure such as this, where the network is composed of crystal junctions connecting the fibrillar crystals [21]. The presence of these junctions in the fiber suggests that the network is not entirely destroyed during the drawing process. Instead, a three-dimensional network structure in UHMWPE fibers is maintained throughout processing and present in the drawn fiber. The presence of the three-dimensional network in UHMWPE fibers is interesting because this sort of fibril connection is not captured in the traditional schematic of perfectly aligned fibrils throughout the available micromechanics models. The network of fibrils, a mesoscale structure, may significantly affect the load pathway of fibers in tension by providing a physical junction between adjacent fibrils.

The AFM images of the Post-Draw fiber in Fig. 9C reveal a more intimate contact between microfibrils with less void space between surface microfibrils. The individual microfibrils appear to be stuck together making it difficult to distinguish junctions between microfibrils in the same way seen on the Precursor fiber. However, close inspection of a gap between fibrils in the upper left corner of Fig. 9C shows several microfibrils clearly bridging the void space slightly off-axis. These fibrils appear to be evidence of a network in the Post-Draw fibers, providing proof that the three-dimensional network persists in highly drawn fibers.

Fig. 9D is a higher magnification image of the Post-Draw fiber surface. Clear evidence of the onset of the formation of epitaxial crystallization is observed. Small lamellar structures spanning multiple microfibrils are clearly evident. Classic shish-kabob morphology can also be seen, suggesting that the large scale epitaxial growth observed on the surface of the low denier S130 fiber started out as chain folded lamella nucleating on individual microfibrils. The comparison of the surface morphologies of the Post-Draw and Precursor fiber suggest that advancement of the drawing process at elevated temperatures has lead to melting of metastable structures. Heating during drawing might not only result in the presence of epitaxial crystals, but might also promote

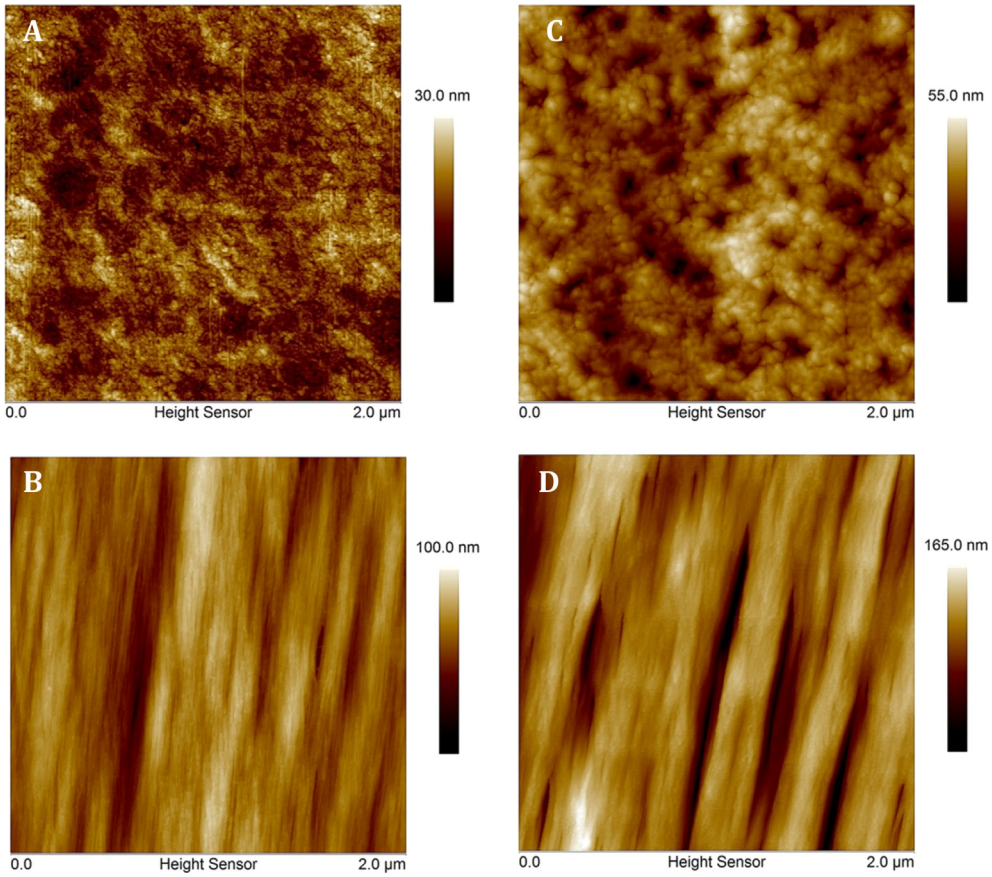

Fig. 11. AFM images of microtomed surface. A) Axial image of Precursor fiber. B) Image of Precursor fiber interior microtomed along the fiber axis. C) Axial image of Post-Draw fiber. D) Image of Post-Draw fiber microtomed along the fiber axis.

adhesion between microfibrils. The closer packing seen in the Post-Draw fiber seems to be a result of surface melting which may act as a sintering process resulting in increased fibrillar adhesion, in a manner similar to macroscopic processing of individual fibers into UHMWPE tapes [47].

To this point, the observations of changing surface morphology between the Precursor and Post-Draw fiber have been mostly qualitative. Logic would dictate that changes in structure and thus mechanical properties would be accompanied by changes in the fundamental structural unit, the microfibril. In the same manner measurements were performed for the S130 fiber, microfibril widths in the Precursor and Post-Draw fiber were also measured. The resulting plots are shown in Fig. 10. The change in microfibril distribution reveals important structural transformations that occur during the drawing process of UHMWPE fibers. All three types of fiber have an average microfibril size between 20 and 40 nm. However, the relative number of microfibrils smaller and larger than this average range significantly narrows upon increased drawing. This transformation is likely due to consolidation resulting from the advancement of the drawing process required to achieve low denier fibers. During the drawing process the smaller microfibrils are able to carry less load, are less thermally stable and likely fracture and melt, either reorganizing into larger microfibrils or to form lamellar crystals. Likewise, the larger microfibrils reduce in diameter as they are drawn, decreasing the number of thicker fibrils. The narrowing of the microfibril diameter distribution, about 20–40 nm average, reflects the balance that is struck between melting and breaking of microfibrils below a critical diameter and drawing of thicker microfibrils. In addition to increases in crystalline perfection and orientation, the drawing process increases the uniformity with respect to microfibril diameter, which should lead to a more uniform distribution of load across the diameter of the fiber.

3.5. Microtomed fibers

If drawing at elevated temperatures promotes interfibrillar adhesion and closer packing, then this phenomenon should not be limited to the surface, but found throughout the fiber as well. Fibers were microtomed both perpendicular and along the fiber axis to reveal the axial and radial structure respectively. The fibers embedded in a Spurr resin were subsequently imaged by AFM and the results presented in Fig. 11, are consistent with what has been observed from analysis of the filament surfaces. Fig. 11A is an image of the cross section of the Precursor fiber where small ends of the microfibrils can be seen. It is also interesting to note the variation in microfibril end density within the field of view, suggesting the presence of significant void space. Fig. 11B is an image of the filament center from a sample that has been microtomed along the filament axis. In this image, individual microfibrils with an average diameter of 27 nm are clearly resolvable, and clear evidence of oval shaped voids is noticed. Fig. 11C and D shows the microtomed surfaces for the Post-Draw fiber. Examination of Fig. 11C shows that individual microfibrils have been consolidated into larger bundles. Likewise, clear, discrete voids are present with an average diameter of approximately 150 nm Fig. 11D shows a similar morphology to that seen on the surface of the Post-Drawn filament with an average microfibril width of 33 nm.

Of interest are the voids seen throughout the fiber thickness and particularly their evolution between the Precursor and Post-Drawn fibers. Voids are on a scale comparable to an individual microfibril diameter in the axial images of the Precursor filament (Fig. 11A). However, in the Post-Drawn filaments voids 100's of nm in size are seen in abundance, while individual microfibrils have been consolidated into bundles. Furthermore, examining the microtomed cross-sections along the axis of the Post-Draw filament indicates that the drawing process has increased the aspect ratio of these voids, with a major axis dimension in excess of a micron in length. These results are consistent with literature values of void sizes calculated in highly drawn UHMWPE [18,48].

It should be noted, in contrast to the image in Fig. 9D, no clear evidence of large arrays of epitaxial structures is observed in the interior of the Post-Draw filament (Fig. 11D). This is likely due to the fact that formation of these large arrays requires significant free space to grow, which is severely limited within the interior of the filament. Instead, the combination of drawing and melting seems to consolidate the microfibrils into bundles and in doing so, also consolidate the voids within the interior of the filament. This is a dramatic change in structure on the mesoscale that has implications for how load is distributed within the filament. The increase in uniformity with respect to both average microfibril diameter, and the increase in adhesion between microfibrils and their consolidation into larger bundles of uniform diameter is expected to result in a more uniform distribution of stresses when loaded in tension [49]. This interpretation is consistent with the tensile testing data. However, the effect of adhesion between microfibrils and consolidation of nanoscale voids into large microvoids on filament performance when loaded in shear and in transverse compression is not clear. Elucidation of these questions will be the subject of future investigation.

4. Conclusions

The sub-filament meso/nanostructure of UHMWPE fibers that have undergone multiple stages of drawing were explored through the use of AFM and WAXD. Tensile strength was shown to increase with the addition of a second drawing step at an elevated temperature, although little change in crystal orientation or overall crystallinity was observed. Changes in key morphological features on the fiber surface and interior as a function of process history were identified. Microfibrils, identified as the fundamental structural unit, were examined and the characteristic distribution of widths were quantified for fibers of progressively higher degrees of drawing. The distribution of microfibril widths was shown to significantly narrow with increasing draw, with an average diameter on the order of ~35 nm. WAXD experiments show that the effective scattering domain size along the (110), (200), and (020) crystallographic zones increases with increased drawing, reflecting an improvement in the overall crystalline perfection. AFM observations revealed that these microfibrils form a 3-dimensional network, rather than the bundles of continuous microfilaments often depicted in the literature.

Examination of the fiber surfaces shows arrays of epitaxial lamella spanning multiple microfibrils for fibers that have undergone a second drawing step at elevated temperature. Annealing experiments show that these structures undergo thickening at temperatures greater than 130 °C, which is consistent with the behavior of chain-folded Polyethylene crystals as opposed to low molecular weight wax or processing aids. The results imply that these fibers were processed at temperatures high enough cause melting of less stable ordered phases and/or surface melting of extended chain crystals that make up the microfibrils during the final stage of drawing. AFM examination of the longitudinal and axial cross sections of each fiber type show that the interior microfibrils undergo consolidation into bundles with increased drawing at elevated temperatures. It is believed that the observed improvement in crystalline perfection and the consolidation of individual microfibrils into macroscale bundles with uniform diameter reduces the number of critical defects and creates a more uniform distribution of stress through the fiber cross section under tensile loading conditions.

Acknowledgments

The authors would like to thank Laurie Wagner and Steve Correale of Honeywell International Inc., and Dr. Nicolas Alvarez at Drexel University for their valuable discussion and insight. We would also like to thank Danning Zhang at the University of Delaware for her help acquiring Micro-CT images of the fibers. Research was sponsored by the Army Research Laboratory and was accomplished under Cooperative Agreement Number W911NF-12-2-0022. The views and conclusions contained in this document are those of the authors and should not be interpreted as representing the official policies, either expressed or implied, of the Army Research Laboratory or the U.S. Government. The U.S. Government is authorized to reproduce and distribute reprints for Government purposes notwithstanding any copyright notation herein.

References

[1] Kavesh S, Prevorsek DC. Ultra high strength, high modulus polyethylene spectra fibers and composites. Int J Polym Mater 1995;30:15–56.
[2] Prevorsek DC, Chin HB, Bhatnagar A. Damage tolerance: design for structural integrity and penetration. Compos Struct 1993;23:137–48.
[3] Marissen R. Design with ultra strong polyethylene fibers. Mater Sci Appl 2011;2:319–30.
[4] Zwijnenburg A, Pennings A. Longitudinal growth of polymer crystals from flowing solutions III. Polyethylene crystals in Couette flow. Colloid Polym Sci 1976;254(10):868–81.
[5] Pennings A. Bundle-like nucleation and longitudinal growth of fibrillar polymer crystals from flowing solutions. J Polym Sci: Polym Symp 1977:55–86.
[6] Barham PJ, Keller A. The achievement of high-modulus polyethylene fibers and the modulus of polyethylene crystals. J Polym Sci: Polym Lett Ed 1979;17:591–3.
[7] Barham PJ. Gelation and the production of stiff polyethylene fibres. Polymer 1982;23:1112–22.
[8] Lemstra PJ, van Aerle N, Bastiaansen C. Chain-extended polyethylene. Polym J 1987;19:85–98.
[9] Barham P, Hill M, Keller A. Gelation and the production of surface grown polyethylene fibres. Colloid Polym Sci 1980:899–908.
[10] Crist B. The ultimate strength and stiffness of polymers. Ann Rev Mater Sci 1995;25:295–323.
[11] Crist B, Ratner MA, Brower AL, Sabin JR. Ab initio calculations of the deformation of polyethylene. J Appl Phys 1979;50(10):6047–51.
[12] Wool RP, Bretzlaff RS, Li BY, Wang CH, Boyd RH. Infrared and Raman spectroscopy of stressed polyethylene. J Polym Sci Part B: Polym Phys 1986;24:1039–66.
[13] Fu Y, Chen W, Pyda M, Londono D, Annis B, Boller A, et al. Structure-property analysis for gel-spun, ultrahigh molecular mass polyethylene fibers. J Macromol Sci – Phys 1996;B35:37–87.
[14] Schaper A, Zenke D, Schulz E, Hirte R, Taege M. Structure-property relationships of high-performance polyethylene fires. Phys Stat Sol A – Appl Res 1989;116(1):179–95.
[15] Magonov SN, Sheiko SS, Deblieck R, Moller M. Atomic force microscopy of gel-drawn molecular weight polyethylene. Macromolecules 1993;26:1380–6.
[16] Grubb D, Keller A. Thermal contraction and extension in fibrous crystals of polyethylene. Colloid Polym Sci 1978;256:218–33.
[17] Grubb DT, Li ZF. Molecular stress distribution and creep of high modulus polyethylene fibres. Polymer 1992;33(12):2587–97.
[18] Hu W-G, Schmidt-Rohr K. Characterization of ultradrawn polyethylene fibers by NMR: crystallinity, domain sizes and a highly mobile second amorphous phase. Polymer 2000;41:2979–87.
[19] Ohta Y, Murase H, Hashimoto T. Structural development of ultra-high strength polyethylene fibers: transformation from kebabs to shishs through hot-drawing process of gel-spun fibers. J Polym Sci Part B: Polym Phys 2010;48:1861–72.
[20] Hoogsteen W, van der Hooft R, Postema A, ten Brinke G, Pennings AJ. Gel-spun polyethylene fibres part 1: influence of spinning temperature and spinline stretching on morphology and properties. J Mater Sci 1988;23:3459–66.

[21] Barham PJ, Keller A. High-strength polyethylene fibres from solution and gel spinning. J Mater Sci 1985;20(7):2281–302.
[22] Pennings A, Smook J, de Boer J, Gogolewski S, van Hutten P. Process of preparation of and properties of ultra-high strength polyethylene fibers. Pure Appl Chem 1983;55(5):777–98.
[23] Wawkuschewski A, Cantow HJ, Magonov SN, Hewes JD, Kocur MA. Scanning force microscopy of high modulus polyethylene fibers. Acta Polym 1995;46(2):168–77.
[24] Strawhecker KE, Cole DP. Morphological and local mechanical surface characterization of ballistic fibers via AFM. J Appl Polym Sci 2014;131.
[25] Grubb DT. A structural model for high-modulus polyethylene derived from entanglement concepts. J Polym Sci: Polym Phys Ed 1983;21:165–88.
[26] Barham PJ, Arridge R. A fiber model of highly oriented polyethylene. J Polym Sci: Polym Phys Ed 1977;15:1177–88.
[27] Arridge R, Barham PJ. A fibre composite model of drawn crystalline polymers. Polymer 1978;19:654–8.
[28] Gao X, Jensen R, Li W, Deitzel J, McKnight SH, Gillespie Jr JW. Effect of fiber surface texture created from silane blends on the strength and energy absorption of the glass fiber/epoxy interphase. J Compos Mater 2008;42(5):513–34.
[29] Rockwell J. High velocity impact of dyneema laminates of varying size. University of Delaware, Civil Engineering; 2014 [Thesis].
[30] ASTM D3822/D3822M-14. Standard test method for tensile properties of single textile fibers. West Conshohocken, PA: ASTM International; 2014.
[31] ASTM D1577–07(2012). Standard test methods for linear density of textile fibers. West Conshohocken, PA: ASTM International; 2012.
[32] Kavesh S, Prevorsek DK. Patent No. 4413110. USA; 1982.
[33] Quantitative Mechanical Property Mapping at the Nanoscale with PeakForce QNM. Bruker. Appl Note 128: 1–12.
[34] Paris S, Hasinoff SW, Kautz J. Local laplacian filters: edge-aware image processing with a laplacian pyramid. ACM Trans Graph – Proc ACM SIGGRAPH 2011 2011;30(4).
[35] Hu X-P, Hsieh Y-L. Crystallite sizes and lattice distortions of gel-spun ultra-high molecular weigh polyethylene fibers. Polym J 1998;30(10):771–4.
[36] Hsieh Y-L, Ju J. Melting behavior of ultra-high modulus and molecular weight polyethylene fibers. J Appl Polym Sci 1994;53:347–54.
[37] Litvinov VM, Xu J, Melian C, Demco DE, Moller M, Simmelink J. Morphology, chain dynamics, and domain sizes in highly drawn gel-spun ultrahigh molecular weight polyethylene fibers at the final stages of drawing by SAXS, WAXS, and 1H solid-state NMR. Macromolecules 2011;44:9254–66.
[38] Alexander LE. X-ray diffraction methods in polymer science. New York: Wiley-Interscience; 1969.
[39] Frye CJ, Ward IM, Dobb MG, Johnson DJ. Direct measurements of crystallite size distribution in ultra-high modulus polyethylene fibres. Polym Commun 1979;20:1310–2.
[40] Lewin M, Pearce EM. Handbook of fiber chemistry. New York: Marcel Dekker, Inc.; 1998.
[41] Northolt M, Hout R. Elastic extension of an oriented crystalline fibre. Polymer 1985;26:310–6.
[42] Warner SB. Fiber science. Upper Saddle River, NJ: Prentice Hall; 1995, ISBN 0024245410.
[43] Van Hutton P, Koning C, Pennings A. The plastic deformation of ultra-high molecular weight polyethylene. J Mater Sci 1985;20:1556–70.
[44] Bhatnagar A, Arvidson BD, Hurst DA, Powers DF, Steenkamer DA. Patent No. US20080064280. USA; 2008.
[45] Geil PH. Polymer single crystals. Huntington, NY: Robert E. Krieger Publishing Company; 1973, ISBN 0882750887.
[46] Wunderlich B, Melillo L. Surface recrystallization of polyethylene extended-chain crystals. Science 1966;154(3754):1329–30.
[47] Rein DM, Vaykhansky L, Khalfin RL, Cohen Y. Controlling the properties of single-polymer composites by surface melting of the reinforcing fibers. Polym Adv Technol 2002;13:1046–54.
[48] Smith JB, Davies GR, Capaccio G, Ward IM. The dynamic mechanical behavior of ultra-high modulus linear polyethylene. J Polym Sci: Polym Phys Ed 1975;13:2331–43.
[49] Chou T-W. Microstructural design of fiber composites. Cambridge: Cambridge University Press; 1992.